Rapid optimization of large-scale luminescent solar concentrators: evaluation for adoption in the built environment

Merkx, E. P.J.; Ten Kate, O. M.; Van Der Kolk, E.

DOI
10.1364/OE.25.00A547

Publication date
2017

Document Version
Final published version

Published in
Optics Express

Research Article | Vol. 25, No. 12 | 12 Jun 2017 | OPTICS EXPRESS A547
Optics EXPRESS

Rapid optimization of large-scale luminescent solar concentrators: evaluation for adoption in the built environment

E. P. J. Merkx,[1,*] O. M. ten Kate,[2] and E. van der Kolk[1]

[1] *Fundamental Aspects of Materials and Energy, Delft University of Technology, Mekelweg 15, 2629 JB Delft, the Netherlands*
[2] *Department of Chemical Engineering, Delft University of Technology, Van der Maasweg 9, 2629 HZ Delft, the Netherlands*
[*] *e.p.j.merkx@tudelft.nl*

Abstract: The phenomenon of self-absorption is by far the largest influential factor in the efficiency of luminescent solar concentrators (LSCs), but also the most challenging one to capture computationally. In this work we present a model using a multiple-generation light transport (MGLT) approach to quantify light transport through single-layer luminescent solar concentrators of arbitrary shape and size. We demonstrate that MGLT offers a significant speed increase over Monte Carlo (raytracing) when optimizing the luminophore concentration in large LSCs and more insight into light transport processes. Our results show that optimizing luminophore concentration in a lab-scale device does not yield an optimal optical efficiency after scaling up to realistically sized windows. Each differently sized LSC therefore has to be optimized individually to obtain maximal efficiency. We show that, for strongly self-absorbing LSCs with a high quantum yield, parasitic self-absorption can turn into a positive effect at very high absorption coefficients. This is due to a combination of increased light trapping and stronger absorption of the incoming sunlight. We conclude that, except for scattering losses, MGLT can compute all aspects in light transport through an LSC accurately and can be used as a design tool for building-integrated photovoltaic elements. This design tool is therefore used to calculate many building-integrated LSC power conversion efficiencies.

OCIS codes: (080.1753) Computation methods; (350.6050) Solar energy; (220.1770) Concentrators; (160.2540) Fluorescent and luminescent materials.

References and links

1. F. Frontini, P. Bonomo, A. Chatzipanagi, G. Verberne, M. van den Donker, K. Sinapis, and W. Folkerts, "BIPV product overview for solar facades and roofs," Tech. Rep. (2015).
2. W. H. Weber and J. Lambe, "Luminescent greenhouse collector for solar radiation," Appl. Opt. **15**, 2299–2300 (1976).
3. J. S. Batchelder, A. H. Zewai, and T. Cole, "Luminescent solar concentrators 1: theory of operation and techniques for performance evaluation," Appl. Opt. **18**, 3090–3110 (1979).
4. L. Desmet, A. J. M. Ras, D. K. G. de Boer, and M. G. Debije, "Monocrystalline silicon photovoltaic luminescent solar concentrator with 4.2% power conversion efficiency," Opt. Lett. **37**, 3087–3089 (2012).
5. J. C. Goldschmidt, M. Peters, A. Bösch, H. Helmers, F. Dimroth, S. W. Glunz, and G. Willeke, "Increasing the efficiency of fluorescent concentrator systems," Sol. Energ. Mater. Sol. Cells **93**, 176–182 (2009).
6. M. de Jong, W. Kesteloo, and E. van der Kolk, "Deposition of luminescent NaCl:Tm^{2+} thin films with a Tm concentration gradient using RF magnetron sputtering," Opt. Mater. **46**, 149–153 (2015).
7. J. S. Batchelder, A. H. Zewail, and T. Cole, "Luminescent solar concentrators 2: experimental and theoretical analysis of their possible efficiencies," Appl. Opt. **20**, 3733–3754 (1981).
8. A. Chatten, K. Barnham, B. Buxton, N. Ekins-Daukes, and M. Malik, "A new approach to modelling quantum dot concentrators," Sol. Energ. Mater. Sol. Cells **75**, 363–371 (2003).
9. L. Fang, T. S. Parel, L. Danos, and T. Markvart, "Photon reabsorption in fluorescent solar collectors," J. Appl. Phys. **111**, 076104 (2012).
10. I. Papakonstantinou and C. Tummeltshammer, "Fundamental limits of concentration in luminescent solar concentrators revised: the effect of reabsorption and nonunity quantum yield," Optica **2**, 841 (2015).
11. A. Earp, G. Smith, P. Swift, and J. Franklin, "Maximising the light output of a luminescent solar concentrator," Sol. Energy **76**, 655–667 (2004).

#282735 https://doi.org/10.1364/OE.25.00A547
Journal © 2017 Received 12 Dec 2016; revised 8 Mar 2017; accepted 13 Mar 2017; published 19 May 2017

Optics EXPRESS

12. A. A. Earp, G. B. Smith, J. Franklin, and P. Swift, "Optimisation of a three-colour luminescent solar concentrator daylighting system," Sol. Energ. Mater. Sol. Cells **84**, 411–426 (2004).
13. J. Sansregret, J. M. Drake, W. R. L. Thomas, and M. L. Lesiecki, "Light transport in planar luminescent solar concentrators: the role of DCM self-absorption," Appl. Opt. **22**, 573–577 (1983).
14. M. Carrascosa, S. Unamuno, and F. Agullo-Lopez, "Monte Carlo simulation of the performance of PMMA luminescent solar collectors," Appl. Opt. **22**, 3236–3241 (1983).
15. V. Sholin, J. D. Olson, and S. A. Carter, "Semiconducting polymers and quantum dots in luminescent solar concentrators for solar energy harvesting," J. Appl. Phys. **101**, 123114 (2007).
16. L. R. Wilson, B. C. Rowan, N. Robertson, O. Moudam, A. C. Jones, and B. S. Richards, "Characterization and reduction of reabsorption losses in luminescent solar concentrators," Appl. Opt. **49**, 1651–1661 (2010).
17. D. Şahin, B. Ilan, and D. F. Kelley, "Monte-Carlo simulations of light propagation in luminescent solar concentrators based on semiconductor nanoparticles," J. Appl. Phys. **110**, 033108 (2011).
18. S. R. Wilton, M. R. Fetterman, J. J. Low, G. You, Z. Jiang, and J. Xu, "Monte Carlo study of PbSe quantum dots as the fluorescent material in luminescent solar concentrators," Opt. Express **22**, A35 (2014).
19. A. Kerrouche, D. A. Hardy, D. Ross, and B. S. Richards, "Luminescent solar concentrators: from experimental validation of 3D ray-tracing simulations to coloured stained-glass windows for BIPV," Sol. Energ. Mater. Sol. Cells **122**, 99–106 (2014).
20. V. I. Klimov, T. A. Baker, J. Lim, K. A. Velizhanin, and H. McDaniel, "Quality factor of luminescent solar concentrators and practical concentration limits attainable with semiconductor quantum dots," ACS Photonics p. acsphotonics.6b00307 (2016).
21. M. G. Debije and Verbunt, Paul P. C., "Thirty years of luminescent solar concentrator research: solar energy for the built environment," Adv. Energy Mater. **2**, 12–35 (2012).
22. O. M. ten Kate, K. M. Hooning, and E. van der Kolk, "Quantifying self-absorption losses in luminescent solar concentrators," Appl. Opt. **53**, 5238–5245 (2014).
23. Z. Krumer, S. J. Pera, R. J. A. van Dijk-Moes, Y. Zhao, A. F. P. de Brouwer, E. Groeneveld, W. G. J. H. M. van Sark, R. E. I. Schropp, and C. de Mello Donega, "Tackling self-absorption in luminescent solar concentrators with type-II colloidal quantum dots," Sol. Energ. Mater. Sol. Cells **111**, 57–65 (2013).
24. D. Alonso-Álvarez, D. Ross, E. Klampaftis, K. R. McIntosh, S. Jia, P. Storiz, T. Stolz, and B. S. Richards, "Luminescent down-shifting experiment and modelling with multiple photovoltaic technologies," Prog. Photovolt: Res. Appl. **23**, 479–497 (2015).
25. I. Coropceanu and M. G. Bawendi, "Core/shell quantum dot based luminescent solar concentrators with reduced reabsorption and enhanced efficiency," Nano Lett. **14**, 4097–4101 (2014).
26. Y. Zhao, G. A. Meek, B. G. Levine, and R. R. Lunt, "Near-infrared harvesting transparent luminescent solar concentrators," Adv. Opt. Mater. **2**, 606–611 (2014).
27. F. Meinardi, A. Colombo, K. A. Velizhanin, R. Simonutti, M. Lorenzon, L. Beverina, R. Viswanatha, V. I. Klimov, and S. Brovelli, "Large-area luminescent solar concentrators based on 'Stokes-shift-engineered' nanocrystals in a mass-polymerized PMMA matrix," Nat. Photonics **8**, 392–399 (2014).
28. C. S. Erickson, L. R. Bradshaw, S. McDowall, J. D. Gilbertson, D. R. Gamelin, and D. L. Patrick, "Zero-reabsorption doped-nanocrystal luminescent solar concentrators," ACS Nano **8**, 3461–3467 (2014).
29. J. Bomm, A. Büchtemann, A. J. Chatten, R. Bose, D. J. Farrell, N. L. A. Chan, Y. Xiao, L. H. Slooff, T. Meyer, A. Meyer, W. G. J. H. M. van Sark, and R. Koole, "Fabrication and full characterization of state-of-the-art quantum dot luminescent solar concentrators," Sol. Energ. Mater. Sol. Cells **95**, 2087–2094 (2011).
30. Y. Zhao and R. R. Lunt, "Transparent luminescent solar concentrators for large-area solar windows enabled by massive stokes-shift nanocluster phosphors," Adv. Energy Mater. **3**, 1143–1148 (2013).
31. A. P. Green and A. R. Buckley, "Solid state concentration quenching of organic fluorophores in PMMA," Phys. Chem. Chem. Phys. **17**, 1435–1440 (2015).
32. F. M. Vossen, M. P. Aarts, and M. G. Debije, "Visual performance of red luminescent solar concentrating windows in an office environment," Energy Build. **113**, 123–132 (2016).
33. M. A. Green, K. Emery, Y. Hishikawa, W. Warta, and E. D. Dunlop, "Solar cell efficiency tables (version 40)," Prog. Photovolt: Res. Appl. **20**, 606–614 (2012).
34. M. A. Green, K. Emery, Y. Hishikawa, W. Warta, and E. D. Dunlop, "Solar cell efficiency tables (version 46)," Prog. Photovolt: Res. Appl. **23**, 805–812 (2015). PIP-15-110.
35. M. A. Green, K. Emery, Y. Hishikawa, W. Warta, and E. D. Dunlop, "Solar cell efficiency tables (version 45)," Prog. Photovolt: Res. Appl. **23**, 1–9 (2015). PIP-14-274.
36. M. A. Green, K. Emery, Y. Hishikawa, W. Warta, and E. D. Dunlop, "Solar cell efficiency tables (version 48)," Prog. Photovolt: Res. Appl. **24**, 905–913 (2016).
37. M. A. Green, K. Emery, Y. Hishikawa, W. Warta, and E. D. Dunlop, "Solar cell efficiency tables (version 41)," Prog. Photovolt: Res. Appl. **21**, 1–11 (2013).
38. M. A. Green, K. Emery, Y. Hishikawa, W. Warta, and E. D. Dunlop, "Solar cell efficiency tables (version 44)," Prog. Photovolt: Res. Appl. **22**, 701–710 (2014). PIP-14-093.
39. M. Kanellis, M. M. de Jong, L. Slooff, and M. G. Debije, "The solar noise barrier project: 1. effect of incident light orientation on the performance of a large-scale luminescent solar concentrator noise barrier," Renew. Energy **103**, 647–652 (2017).

Optics EXPRESS

1. Introduction

Building-integrated photovoltaics (BIPVs) are a promising solution for the wide adoption of electricity generation through solar energy. With the trend towards large glass facades in public- and commercial buildings a (semi-) transparent BIPV could expect incorporation in the built environment [1]. A luminescent solar concentrator (LSC) is such a transparent potential BIPV. LSCs were intensely studied during the 1970s [2, 3] and are regaining more interest with the advent of new types of quantum dots (QDs), luminescent dyes and rare-earth materials. The window-like qualities of these new materials, such as letting the shape of the visible spectrum remain unaltered, make them suitable as BIPV. A typical LSC is either a polymer plate (mostly PMMA) doped with luminophores, or a glass sheet carrying a luminescent coating [4–6]. Figure 1 illustrates the luminescent solar concentrating process. Luminescent centers contained in these materials absorb part of the incoming diffuse and direct sunlight, followed by reemission at longer wavelengths. The emitted luminescence is waveguided through the LSC plate to its perimeter, where conventional photovoltaic (PV) cells convert this waveguided light into electricity. As a result, the strip-shaped PV cells will receive sunlight from a larger area than they would when directly exposed to the sun, which enhances their electricity generation. If the luminescent coating is semi-transparent, an electricity generating window ideal for BIPV applications can be achieved.

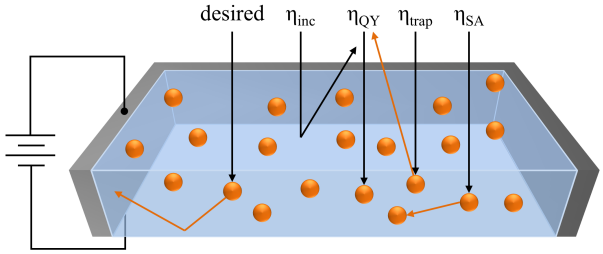

Fig. 1. Schematic cross-section of the working of a single-layer LSC. Orange spheres represent the luminescent centers within a transparent medium. PV cells (gray) surround the perimeter of the concentrator plate. 'desired' shows the desired concentrating process without any losses. All other arrows show possible loss mechanisms within an LSC and their associated efficiency: non-unity incoupling due to reflection losses (η_{inc}), non-unity quantum yield due to non-radiative decay (η_{QY}), non-unity trapping due to escape-cone losses (η_{trap}) and losses due to self-absorption (η_{SA}). Losses due to scattering within the LSC are not considered in this work and therefore not depicted.

In many LSCs the range of absorbed and emitted wavelengths overlap. Reabsorbed light is often not reemitted with unity efficiency, and, even when reemitted, typically has a 25 % chance of being lost through the escape-cone. This parasitic self-absorption therefore yields increasing losses with bigger LSCs. Hence, an accurate and fast treatment of the effect of self-absorption on LSC efficiency is needed to both calculate LSC efficiency and to optimize this efficiency for large LSCs intended for BIPV use.

Light transport within an LSC was described using a series of absorption and reemission events by Batchelder *et al.* [3, 7], who referred to it as multiple-generation self-absorption. The analytical equations presented were solved for the simplified case of a semi-infinite rod. Most modern approaches to quantification of self-absorption are carried out with thermodynamic calculations [8–10], analytical models based on the Beer-Lambert law [11, 12], or using Monte Carlo (MC) simulations [13–20], also referred to as raytracing. While MC simulations are relatively easy to implement, they rely on random numbers to calculate physical effects. As a result, a high demand is put on the collection of ever larger statistics as the size of the simulated

Optics EXPRESS

system increases. In materials featuring a large amount of self-absorption and a high quantum yield η_{QY}, tracing a single photon in a system will take longer with increasing optical density. In this work we show that these two factors result in a long calculation time when optimizing a realistically-sized LSC. Furthermore, we present a method that fully describes light transport within an LSC. This method can quickly and accurately optimize large-size LSCs through the variation of luminophore concentration.

This paper consists of three parts. In the first part we present a model that calculates all light transport processes within an LSC, based on multiple-generation light transport (MGLT). We will check the correctness and internal consistency of the model by comparing calculations with an MC model using the same input data. Here the calculation speed when optimizing large, high η_{QY} LSCs using MGLT as opposed to MC will be made evident. Results are presented for well-known luminescent polymers, like Lumogen Red305 as well as state-of-the-art polymer and QD-based LSCs, where all required data was published. In the second part we put the model to use by optimizing the luminophore concentration for the presented materials, both for lab-scale ($100\,cm^2$) and BIPV-scale ($1\,m^2$) LSCs. In this optimization the potentially beneficial effects of self-absorption when η_{QY} of an LSC is near unity will be shown. Finally, the potential as BIPV window is evaluated for all presented LSCs, after optimizing their optical efficiency.

2. Multiple-generation light transport

To characterize LSC performance an often used metric is the optical efficiency η [21]. η gives the ratio of incident solar photons to photons collected at the side. In case of a waveguide without self-absorption, scattering or coupling losses at the perimeter

$$\eta_{ideal} = \eta_{inc}\eta_{LHE}\eta_{QY}\eta_{trap} \,. \tag{1}$$

Here η_{inc} is the incoupling efficiency: the amount of light entering the LSC, η_{LHE} the fraction of sunlight absorbed over the thickness of the LSC, η_{QY} the photoluminescent quantum yield of the luminescent centers and η_{trap} the fraction of light which remains trapped within the LSC after reemission.

Light incident on an LSC first has to enter the waveguide; here losses are quantified by the angular-dependent reflection, described by the Fresnel equations. For simplicity and comparability with earlier computations and experiments, the remainder of this work considers uniform unpolarized light entering perpendicular to the LSC's surface. In this case, the incoupling efficiency is given by

$$\eta_{inc} = 1 - \left|\frac{n_1 - n_2}{n_1 + n_2}\right|^2 \,, \tag{2}$$

with n_i the wavelength-independent refractive indices for the two media the light passes through, yielding for example $\eta_{inc} \approx 96\,\%$ for light transmitting from air to PMMA.

To contribute to photon transport to the edges, light entering the LSC has to be absorbed over the thickness t of the LSC. The light harvesting efficiency η_{LHE} gives the fraction of solar light which will be absorbed by the LSC after entering:

$$\eta_{LHE} = \frac{\int^{\lambda} S(\lambda)(1 - \exp(-\alpha(\lambda)t))\,\mathrm{d}\lambda}{\int^{\lambda} S(\lambda)\,\mathrm{d}\lambda} \,. \tag{3}$$

Here $S(\lambda)$ is the spectrum of the incident light expressed in amount of photons per wavelength and $\alpha(\lambda)$ the absorption coefficient per distance. The integration is done over the wavelength-domain λ of interest, in this work 280 nm to 4000 nm.

The absorbed fraction $N_{absorbed}$ from an initial count of solar photons N will therefore be $N_{absorbed} = \eta_{inc}\eta_{LHE}N$. $N_{absorbed}$ can now be converted by the luminescent centers. Following the

Optics EXPRESS

derivation by Ten Kate *et al.* [22], conversion happens with the normalized emission spectrum of the LSC Φ_{em} as a rate of power

$$\frac{\Phi_{\text{em}}(\lambda)}{\lambda} = \frac{1}{\lambda}\frac{\epsilon(\lambda)}{\int^{\lambda}\epsilon(\lambda)\,\mathrm{d}\lambda} \,. \tag{4}$$

The conversion occurs with an efficiency provided by the quantum yield η_{QY}, assumed to be independent of luminophore concentration. Isotropic reemission follows, resulting in a reemission spectrum

$$\sigma_0(\lambda) = \eta_{\text{QY}} N_{\text{absorbed}} \frac{\Phi_{\text{em}}(\lambda)}{\lambda} \,. \tag{5}$$

For an isotropic point emitter, the radiant power $I(s)$, a distance $s = \sqrt{x^2 + y^2}$ away from the emitter, is given by the Beer-Lambert law:

$$I(s) = I_0 \exp(-\alpha s) \,, \tag{6}$$

where I_0 is the intensity of the emitter.

The amount of light absorbed in a circular segment $(s, s + \mathrm{d}s)$ equals the derivative of the Beer-Lambert law with respect to s. The corresponding absorption density factor $a(s, \lambda)$ per unit area, a distance s away from the emission center, is therefore

$$a(s, \lambda) = \frac{\alpha(\lambda)\exp(-\alpha(\lambda)s)}{2\pi s} \,. \tag{7}$$

$a(s, \lambda)$ is a density, independent of the initial intensity, hence I_0 is omitted.

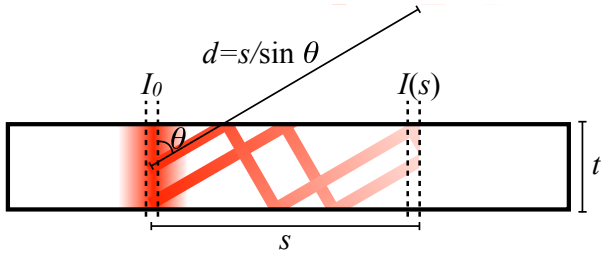

Fig. 2. The two rays drawn are both emitted at an angle θ from different depths within the LSC. Both rays have to travel the same distance $s/\sin(\theta)$ to reach a column at a distance s, viewed from the top of the LSC. The radiant power $I(s)$ of the light from both rays is therefore equal at s, independent of the depth the light was emitted from.

To simplify the description of light transport through an LSC using this circular emission, two aspects need to be taken into account. First, the path length of light traveling to the perimeter has to be independent of depth. Figure 2 shows that, to reach a distance s horizontally, light has to traverse a distance $\frac{s}{\sin\theta}$ in an LSC plate, independent of emission depth. Second, the path the light takes needs to be independent of the polar emission angle θ. Redefining $\alpha(\lambda)$ to account for all possible emission angles, limited by the escape-cone, yields the effective absorption coefficient

$$\alpha'(\lambda) = \frac{\alpha(\lambda)}{\pi - 2\theta_c} \int_{\theta_c}^{\pi-\theta_c} \frac{1}{\sin(\theta)}\,\mathrm{d}\theta \,, \tag{8}$$

where θ_c is the LSC's critical angle.

Optics EXPRESS

The effective absorption coefficient allows us to work with depth- and emission-angle independent columns rather than having to take all separate luminescent centers (points) into account. We can therefore work in a 2D rather than in a 3D plane.

To obtain the reabsorption within a column $\gamma_i(x, y, \lambda)$, light emitted from all other columns within the LSC plane needs to be accounted for. A 2D convolution describes this problem. Convolving the absorption density factor and emission distribution provides

$$\gamma_i(x, y, \lambda) = (\eta_{\text{trap}} + \eta_{\text{CA}}(\lambda))\sigma_i(x, y, \lambda) * *a(x, y, \lambda) \ . \tag{9}$$

Here η_{trap} is the trapping efficiency and η_{CA} the cone absorption efficiency.

η_{trap} is defined as the ratio of light that will be subject to total internal reflection within the LSC plane after reemission. For an LSC in air

$$\eta_{\text{trap}} = \sqrt{1 - \frac{1}{n_2^2}} \ . \tag{10}$$

For PMMA with $n_2 \approx 1.5$ this means that the probability of a photon entering the escape-cone is around 25 %.

η_{CA} provides a measure to account for light that is emitted within the escape-cone but will be reabsorbed before escaping through the LSC's surface [22].

$$\eta_{\text{CA}}(\lambda) = \frac{1}{t} \int_0^t \int_0^{\theta_c} \left(1 - e^{-\alpha(\lambda) z / \cos\theta}\right) \sin\theta \, \mathrm{d}\theta \, \mathrm{d}z \ . \tag{11}$$

Reabsorbed light can be emitted again to a next generation $i + 1$. Similar to Eq. (5), we sum over all absorbed photons and emit with the normalized emission spectrum as a rate of energy. Taking the quantum yield into account, this yields

$$\sigma_{i+1} = \eta_{\text{QY}} \frac{\Phi_{\text{em}}(\lambda)}{\lambda} \int^{\lambda} \lambda \gamma_i(x, y, \lambda) \, \mathrm{d}\lambda \ . \tag{12}$$

The process of reemission and reabsorption continues for many generations i until all photons have either escaped through the escape-cone, have been quenched, or have been collected at the LSC sides. In order to retrieve the amount of collected photons $C_i(\lambda)$ at the sides, we can simply take the difference between the emitted and the absorbed intensity of a generation over the entire LSC surface A_{LSC}. When we correct for escape-cone losses this yields

$$C_i(\lambda) = \eta_{\text{trap}} \lambda \iint_{A_{\text{LSC}}} \left(\sigma_i - \frac{1}{\eta_{\text{trap}} + \eta_{\text{CA}}} \gamma_i\right) \mathrm{d}x \, \mathrm{d}y \ . \tag{13}$$

The total number of collected photons C_Σ can be acquired through summation over all generations and integration over the wavelengths of interest.

With C_Σ the optical efficiency η from the MGLT model is calculated using

$$\eta = \eta_{\text{inc}} \eta_{\text{LHE}} \eta_{\text{QY}} \eta_{\text{trap}} \eta_{\text{SA}} = \eta_{\text{inc}} \eta_{\text{LHE}} \frac{C_\Sigma}{N_{\text{absorbed}}} \ . \tag{14}$$

To summarize, using only the experimentally measured absorption and emission spectra, index of refraction and quantum yield of an LSC material, the complete light transport through an LSC can be calculated by using multiple generations of reemission and reabsorption of light. It is important to note that the required absorption coefficient $\alpha(\lambda)$ is measured under the lowest

Optics EXPRESS

possible luminophore concentration. $\alpha(\lambda)$ measured under high concentrations might cause self-absorption within the material to yield a different spectrum than the real absorption spectrum of the luminophore. Losses due to scattering are not included in the model as presented, but can to a first order be estimated using an additional absorption term, in a similar fashion as presented in the work by Earp *et al.* [11]. This additional absorption term will not contribute to reemission in later generations. Since no assumption on the geometry of the LSC has been made, the MGLT model is usable for any shape and size of planar LSC window.

3. Monte Carlo simulation

In order to verify the outcomes of the presented MGLT model, MC simulations were carried out. The MC simulations use the same absorption and emission spectra, wavelength-independent refractive indices, and concentration-independent quantum yields as input. A flowchart of the simulation is shown in Fig. 3. To initialize the simulation, a photon P is generated incident on the surface of the LSC. P has a wavelength λ, pseudo-randomly chosen using the AM1.5 direct spectrum as distribution. The photon's initial position is determined by

$$\boldsymbol{x} = \begin{pmatrix} x \\ y \\ z \end{pmatrix} = \begin{pmatrix} \xi_x l \\ \xi_y w \\ t \end{pmatrix}, \tag{15}$$

where l, w and t are the LSC's length, width and thickness respectively. ξ_i is defined as a uniformly distributed random number. Each ξ_i mentioned in this work is a different $\xi_i \in [0, 1]$.

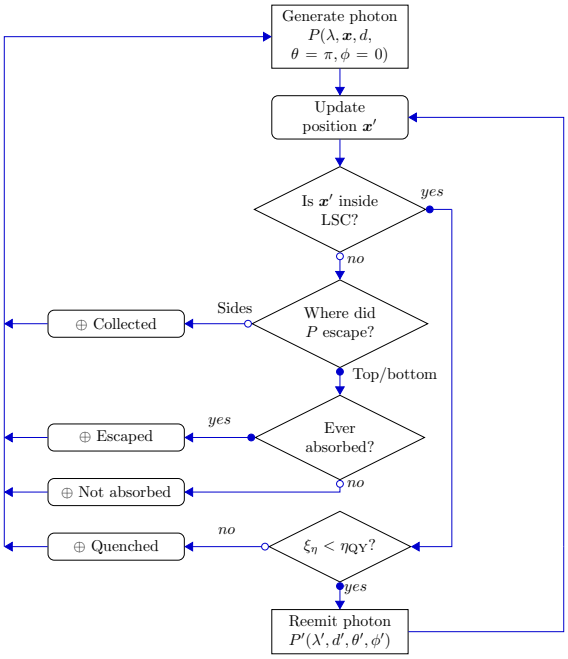

Fig. 3. Schematic representation of the MC simulation.

The path length d the photon will travel is found by rewriting the probability of absorption

$$p = 1 - \exp(-\alpha(\lambda)d) \tag{16}$$

to

$$d = -\frac{1}{\alpha(\lambda)} \log(1 - \xi_d) \ . \tag{17}$$

The photon's new position $\boldsymbol{x}'$ after traveling d, with azimuthal angle ϕ, can be found using

$$\boldsymbol{x}' = \boldsymbol{x} + \begin{pmatrix} d\frac{\sin\phi}{\sin\theta} \\ d\frac{\cos\phi}{\sin\theta} \\ \Delta z \end{pmatrix} \ , \tag{18}$$

where Δz is dependent on the number of reflections

$$R = \left\lfloor \frac{|d\cos\theta + z|}{t} \right\rfloor \ . \tag{19}$$

If the photon is emitted outside of the escape-cone ($\theta_c < \theta < \pi - \theta_c$) and $(\theta - \frac{\pi}{2}) \times \mathrm{Ev}(R) > 0$, then

$$\Delta z = (|d\cos\theta + z| \bmod t) - z \ , \tag{20}$$

with $\mathrm{Ev}(R)$ returning 1 if R is even and -1 otherwise.

Else, if emission is outside of the escape-cone, but $(\theta - \frac{\pi}{2}) \times \mathrm{Ev}(R) < 0$, then

$$\Delta z = t - (|d\cos\theta + z| \bmod t) - z \ . \tag{21}$$

And otherwise, if emission happens within the escape-cone,

$$\Delta z = d\cos\theta \ . \tag{22}$$

$\phi = 0$ and $\theta = \pi$ for the initial photon, providing the same η_{inc} as in the MGLT model. If the photon is absorbed within the LSC, a random number is generated which determines if emission occurs, based on η_{QY}. Upon reemission a new wavelength λ' will be assigned to the photon by inverse transform sampling the LSC's emission spectrum. The photon will also acquire new emission angles

$$\phi' = 2\pi\xi_\phi \ , \tag{23}$$

$$\theta' = \arccos(2\xi_\theta - 1) \ . \tag{24}$$

When the photon exits the LSC through the sides, it is assumed to be collected by the PV cells. Otherwise, the photon has escaped through the escape-cone or has never been absorbed at all. Each simulation runs with $N_{\mathrm{input}} = 10^7$ photons to obtain a proper statistic. The optical efficiency is extracted as

$$\eta = \eta_{\mathrm{inc}} \frac{N_{\mathrm{collected}}}{N} \ . \tag{25}$$

4. Model verification

In order to test the MGLT model, a selection of recent LSC materials was made for which all required data were available as published information. Although research on state-of-the-art materials has already started to shift its attention to Stokes' shift engineering the absorption and emission spectra, dyes featuring significant spectral overlap have also been selected. These materials with spectral overlap can aid in verifying the model's capabilities for quantifying self-absorption. See Data File 1 for the required spectroscopic properties and optical efficiencies of all materials, calculated with both MC and MGLT. All calculations are done on a desktop computer with an Intel i5-6500 CPU clocked at 3.2 GHz.

Optics EXPRESS

When excluding materials with less than 1 % optical efficiency, excellent agreement between the two models is observed. Based on the simulation results from published data (Data File 1), the relative difference $\left(\frac{\eta^{\mathrm{MC}}-\eta^{\mathrm{MGLT}}}{\eta^{\mathrm{MC}}}\right)$ between MGLT and MC for 100 cm^2 plates is 2.1 ± 6.3 %, and for 1 m^2 plates is 4.4 ± 7.7 %. Materials with $\eta < 1$ % have been excluded, as only a very minor difference in absolute calculated efficiency already causes a great increase in the difference in relative efficiency.

To illustrate the in-depth agreement with MC and functionality of the MGLT model, a $10 \times 10 \times 0.5\,\mathrm{cm}^3$ Lumogen Orange (LumoO) [23] LSC plate can be taken as example, since it features a strong self-absorption [see Fig. 4(a)] and a high quantum yield ($\eta_{\mathrm{QY}} = 0.95$).

The self-absorption efficiency η_{SA} does not provide information about whether the photon was lost due to escaping or quenching. Therefore we have chosen to separate η_{SA} into an effective fraction of trapped photons $\eta_{\mathrm{trap\ eff}}$ and an effective luminescent quantum yield $\eta_{\mathrm{QY\ eff}}$. Here

$$\eta_{\mathrm{trap\ eff}} = 1 - \frac{N_{\mathrm{escaped}}}{N_{\mathrm{absorbed}} - N_{\mathrm{quenched}}} \tag{26}$$

and

$$\eta_{\mathrm{QY\ eff}} = 1 - \frac{N_{\mathrm{quenched}}}{N_{\mathrm{absorbed}} - N_{\mathrm{escaped}}}\,. \tag{27}$$

Note that these two effective efficiencies together do not provide the total device efficiency, but only show how great the amount of photons lost due to only escaping or quenching is. Table 1 provides the calculated (effective) efficiencies for each considered aspect of light transport and illustrates that, for each step of the light transportation process, MC and MGLT produce almost identical results.

Table 1. Calculated efficiencies for a $10 \times 10 \times 0.5\,\mathrm{cm}^3$ LumoO LSC using absorption coefficients as reported by Krumer *et al.* [23].

	MC	MGLT
η_{LHE} (%)	6.88	6.88
$\eta_{\mathrm{QY\ eff}}$ (%)	86.4	86.6
$\eta_{\mathrm{trap\ eff}}$ (%)	62.4	62.5
η (%)	3.76	3.76

The exact shape of the spectrum of the collected photons is highly susceptible to small changes in the treatment of physical input parameters, based on a model's assumptions. Therefore, this spectrum can serve as a rigorous test of physical correctness of the MGLT model. Figure 4(a) shows the spectrum transmitted through the perimeter of a LumoO-based LSC for both MC and MGLT. The transmitted spectra for MGLT and MC are almost identical, with MGLT displaying no random noise in the spectrum. The noise seen with MC is a direct consequence of the model's random nature, which would only decrease with a large increase in simulated photons. It should be noted that the spectrum is also the same before normalization, which is a direct consequence of both models yielding the same optical efficiency. A significant redshift is seen even for a window of 100 cm^2. The redshift can be explained by the overlap between absorption and emission, resulting in light emitted within the overlapping spectral area almost never reaching the window's edge.

These simulations can also be used to optimize LSC performance by changing the amount of absorption, which in practice would mean changing the luminophore concentration. Figure 4(b) shows that the majority of light transport takes place in the first generation (0 on the horizontal axis) of light reemission for the MGLT model. In this first generation a higher contribution η_i to

Optics EXPRESS

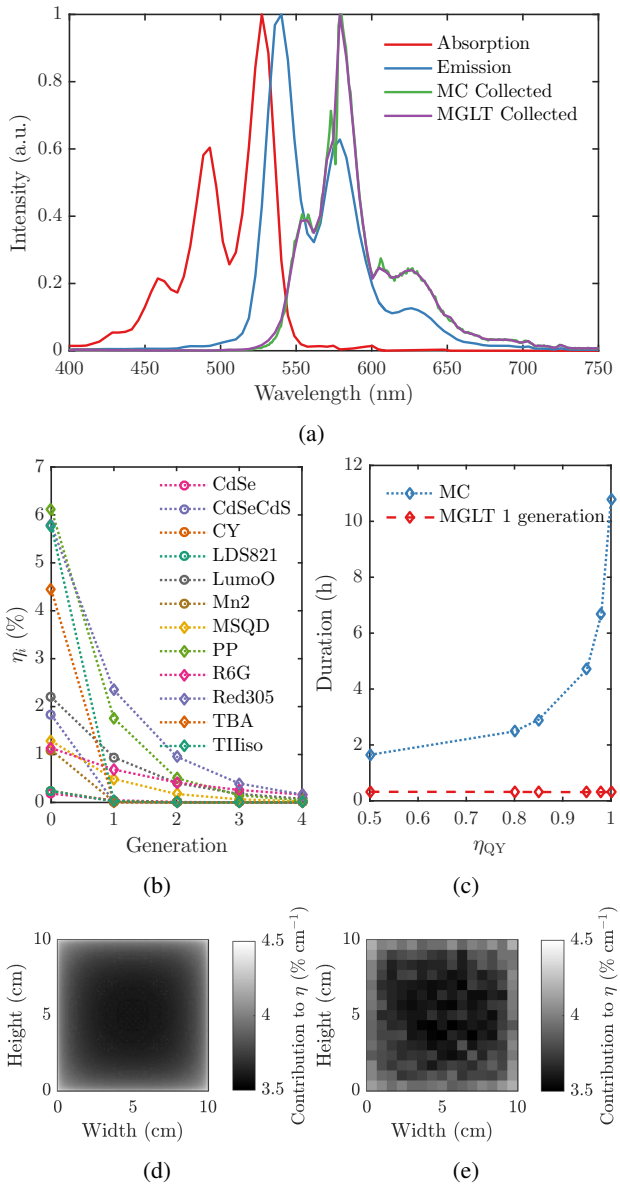

Fig. 4. (a) Comparison between MC and MGLT spectra for the simulated LumoO geometry received at the edges of the LSC. Absorption and emission spectra [23] are shown as well, signifying the large amount of redshift. (b) Optical efficiency per generation for the MGLT model. All materials simulated have absorption coefficients as reported in their respective papers (see Data File 1). Materials with significant spectral overlap have many more generations contributing to the total η due multiple absorption and remission events. (c) Calculation time needed in order to optimize the absorption coefficient for a $10 \times 10 \times 0.5\,\mathrm{cm}^3$ Red305 LSC with different quantum yields. Each datapoint has α ranging from $1 \times 10^{-1}\,\mathrm{cm}^{-1}$ to $1 \times 10^{8}\,\mathrm{cm}^{-1}$. (d) Contribution to the optical efficiency per unit area of the LSC geometry, calculated by MGLT and (e) by MC.

Optics EXPRESS

the total η than in any of the succeeding generations is provided. Calculating just one generation is therefore sufficient for optimization, given $\eta_{QY} < 1$ (see Appendix A). The performance increase MGLT offers over MC is evident from Fig. 4(c). Optimizing a large LSC with MC requires a significant amount of photons to receive enough collected photons for a satisfactory simulation result. When η_{QY} and α rise, a single photon can remain trapped in the LSC for many reabsorption and reemission events, resulting in a long MC simulation time. MGLT, on the other hand, is generation-based, with a constant time required for each generation, resulting in a more constant and predictable time required to calculate optimal α. In MGLT, performance mainly scales with the amount of generations used, but also with how broad the overlap between the absorption and emission spectra is, as the most integration needs to be done across this overlap. Calculating the final efficiency of an optimized LSC is done quickest using a hybrid approach. First the LSC is optimized using one generation of MGLT. The optimal α is then used in an MC simulation to calculate the final efficiency as, for calculation of the full efficiency, MC is usually quicker than MGLT with many (> 5) generations.

Figure 4(d) (MGLT) and Fig. 4(e) (MC) show that the simulations can help acquiring a more detailed view on what part of the LSC contributes most to edge transport. In Figs. 4(d) and 4(e) each unit area receives the same amount of photons; the brightness of that area indicates how many of those photons will eventually reach the perimeter. While the bulk of the LSC provides the most photons, also most light is lost here. These losses can be explained by the distance between the place photons are absorbed and that of their collection. The self-absorption of LumoO causes photons absorbed in the center to become reabsorbed on their way to the perimeter. LumoO's high quantum yield causes most photons to still be reemitted while underway, but each extra absorption event adds to the chance of losing that photon through the escape-cone. Therefore, per unit area, the edge of the LSC contributes slightly more to the amount of collected photons than the bulk. The effect of an LSC's geometry can be studied in detail using MGLT, since the model is formulated around the LSC geometry [see Eq. (9)]. Even after one generation of simulation (not shown) the effect of an LSC's geometry on light transport is clear. With MC a very large amount of photons is necessary to eliminate random noise. In Fig. 4(e) 10^7 photons were binned over a 15×15 grid to reduce noise, resulting in a lesser resolution than observed with MGLT. Around 5×10^{11} photons would need to be simulated with MC to obtain a resolution comparable to MGLT. The geometry appears not to have a high impact on LSC efficiency. It could, however, still be possible to build an aesthetically pleasing LSC with sufficiently high efficiency by optimizing the geometry and opting for a fully transparent center.

Using the models as a design tool can help with understanding how a change in parameters will influence performance [24]. Here the strengths of both models can be used to complement each other. MGLT is formulated using physical laws, without a dependence on the collection of sufficient statistics. Changing one parameter will therefore after a limited amount (usually one) of generations show what influence such a change has on device performance. Once an optimum is found MC can be used to calculate the total device performance.

5. LSC optimization results

Maximizing the optical efficiency of an LSC would result in a maximally efficient BIPV element. Simulations can help designing such an optimal LSC by calculating the absorption coefficient $\alpha^\star$ with maximal optical efficiency $\eta^\star$ for the desired geometry or size.

Table 2 provides us with the results for such optimizations for both a $10 \times 10 \times 0.5\,\mathrm{cm}^3$ and a $100 \times 100 \times 0.5\,\mathrm{cm}^3$ LSC. The value of $\alpha^\star$ is calculated through MGLT, while the optical efficiency $\eta^\star$ with $\alpha = \alpha^\star$ comes from MC. What can be noted from Table 2 is that an optimized lab-scale LSC does not immediately yield an optimized $1\,\mathrm{m}^2$ LSC.

Figure 5 shows GQD as a notable example. The optical efficiency (circles) comes from two competing processes. A higher α means, on the one hand, an increased η_{LHE} (dashed); on the other,

Optics EXPRESS

Table 2. Maximal possible efficiencies for two different LSC sizes for selected materials. $\alpha^{\star}_{\max}$ is the maximal absorption coefficient of the reported spectrum. When $\alpha^{\star}_{\max}$ is denoted as ↑, the highest possible luminophore concentration should be taken (in these calculations limited at $10^5\,\mathrm{cm}^{-1}$), for η_{LHE} has become the dominant factor in determining η for that material.

Material	$\alpha^{\star}_{\max 10\times 10}$ $\left(\mathrm{cm}^{-1}\right)$	$\eta^{\star}_{10\times 10}$ (%)	$\alpha^{\star}_{\max 100\times 100}$ $\left(\mathrm{cm}^{-1}\right)$	$\eta^{\star}_{100\times 100}$ (%)
CdSe [23]	2.9	0.4	1.0	0.1
CdSeCdS [25]	↑	11.8	↑	11.8
CY [26]	7.0	0.2	492.4	0.2
GQD [27]	7.4	2.5	3.3	1
LDS821 [15]	11.3	1.2	7.4	1
LumoO [23]	34.6	4.8	↑	4.7
Mn2 [28]	↑	3.4	↑	3.4
MSQD [29]	25.7	2.0	1343.4	1.7
PP [4]	38.9	11	↑	10.6
R6G [23]	17.0	3.0	7.4	0.7
Red305 [4]	↑	13.5	↑	13.5
TBA [30]	58.8	3.9	203.1	3.9
TIIiso [23]	2424.5	7.6	↑	7.6

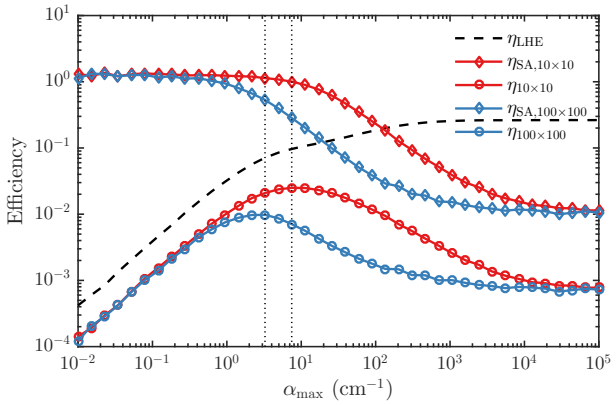

Fig. 5. Optimization track for GQD ($\eta_{\mathrm{QY}} = 0.45$) using two different LSC sizes. The displayed efficiency is the total optical efficiency, calculated through MC. Dotted lines indicate the maxima for the two simulated geometries.

a decreased η_{SA} (diamonds), resulting in a geometry-specific optimum $\alpha_{\max}$. For GQD, a lab-scale device has a maximum of $\alpha^{\star}(\lambda = 474\,\mathrm{nm}) = 7.44\,\mathrm{cm}^{-1}$ with $\eta^{\star}_{10\times 10} = 2.5\,\%$. If that maximum were to be used for the $100 \times 100 \times 0.5\,\mathrm{cm}^3$ window, a lower efficiency of $\eta_{100\times 100} = 0.71\,\%$ would be obtained than when using $\alpha^{\star}(\lambda = 474\,\mathrm{nm}) = 3.26\,\mathrm{cm}^{-1}$ yielding $\eta^{\star}_{100\times 100} = 0.98\,\%$. In line with [11, 12], we can conclude that dye concentration optimization needs to be done for the actual geometry of the LSC, as opposed to a lab-scale device. The combination of MGLT with MC allows us to do such optimization quickly. While Table 2 also shows drastic increases in $\alpha^{\star}_{\max}$ for CY, MSQD and TBA, when comparing $10 \times 10\,\mathrm{cm}^2$ to $100 \times 100\,\mathrm{cm}^2$, the efficiencies for these materials are low throughout the entire range of absorption coefficients. Their efficiencies saturate quickly, since their efficiency is dominated by η_{LHE}. These materials show only a minute increase in η at the reported maximum.

Optics EXPRESS

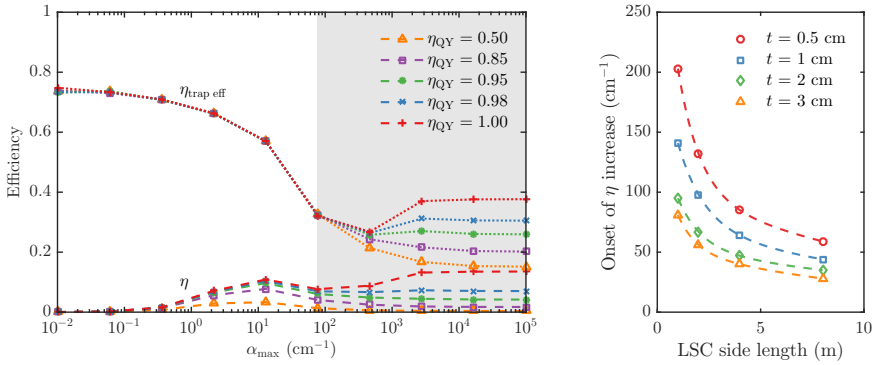

(a) (b)

Fig. 6. (a) Optical efficiency η (dashed) and effective trapping efficiency $\eta_{\text{trap eff}}$ (dotted) in Red305 for increasing quantum yields. The white area indicates the region with low optical density, and the shaded area indicates high optical density. (b) Onset of the increase in η for $\eta_{QY} = 1$ Red305 LSCs of varying sizes and thicknesses. This onset is defined as the point where η starts rising again. Lines are drawn as a guide to the eye.

In self-absorbing materials, the trapping efficiency as defined by Eq. (10) is mostly an upper bound for the amount of photons that do not escape from the LSC's top or bottom surface. Figure 6(a) shows the impact of an increasing absorption coefficient α_{max} on the effective trapping efficiency $\eta_{\text{trap eff}}$ [Eq. (26)] for a 100 cm^2 Red305 with different quantum yields. From Fig. 6(a) we can see that $\eta_{\text{trap eff}}$ can be separated into two regions: low and high optical density.

In the region with low optical density, the expected behavior for a self-absorbing material occurs. Photons are reabsorbed multiple times, and with each reemission there is a $\sim 25\,\%$ chance of entering the escape-cone and escaping through the LSC's surface. A higher α means many reabsorption events, and therefore a higher possibility that a photon will end up escaping. In this region absorption within the escape-cone is outweighed by absorption during total internal reflection. Figure 5 shows that, when considering very low α, the still present escape-cone absorption gives a photon a chance to become absorbed before escaping. This still present trapping yields positive self-absorption, with $\eta_{SA} > 1$. Transport in the region of low optical density is hence governed by reabsorption and remission events during total internal refraction, resulting in a decreasing $\eta_{\text{trap eff}}$ as α_{max} rises.

In the region with high α_{max}, however, we see that $\eta_{\text{trap eff}}$ starts splitting up, depending on η_{QY}. In this region the redshifting of photons starts greatly influencing light transport. A photon will experience many reabsorption events over a short traveled distance. As η_{QY} rises, the probability for the photon to redshift outside of the LSC's absorption spectrum before quenching increases as well. When the photon redshifts outside of the LSCs absorption spectrum it cannot be absorbed again. Transport of the photon is then fully governed by total internal reflection. This leads to the effective trapping efficiency rising to near the theoretical η_{trap} for a large LSC, because when viewed from the perimeter, the absorption and emission spectrum of the LSC do not overlap anymore. Combined with a high η_{QY}, this effect is accentuated, as almost every reabsorbed photon will be reemitted. For a high absorption maximum α_{max}, a local maximum of $\eta_{\text{trap eff}}$ coincides with a high amount of absorbed solar light, yielding a second, higher maximum in optical efficiency for strongly self-absorbing materials, with $\eta_{QY} \approx 1$, like Red305.

In most small-scale experimental setups the second maximum displayed in Fig. 6(a) will not be visible. With high absorption coefficients ($\alpha_{max} > 60\,\text{cm}^{-1}$) luminescence quenching namely occurs [31]. Figure 6(b) shows that as the size or thickness of the LSC increases, the onset

of the second maximum can become visible before luminescence quenching occurs. In large BIPV-scale LSCs of around $4 \times 4\,\mathrm{m}^2$ this effect therefore could become perceivable at realistic concentrations of $\alpha_{\max} < 60\,\mathrm{cm}^{-1}$.

6. Expected BIPV efficiencies

With the hybrid approach of MGLT for optimization and MC for a full efficiency calculation, it is possible to look at how the selected materials would perform as (colored) BIPV windows. Using the data from Table 2 would yield a theoretical maximum efficiency, but also visually opaque windows with potential luminescence quenching. Therefore as design critera we use (*i*) a $100 \times 100 \times 0.5\,\mathrm{cm}^3$ window, (*ii*) maximally 25 % visible light (390 nm to 700 nm) absorption [32], (*iii*) $\alpha_{\max} \leq 60\,\mathrm{cm}^{-1}$ to avoid luminescence quenching.

An important figure of merit is the LSC's power efficiency η_{power}. The power efficiency is the ratio of power produced by the PV cells enclosing the LSC to the incoming sunlight [18]:

$$\eta_{\mathrm{power}} = \frac{I_{\mathrm{sc}} V_{\mathrm{oc}} FF}{P_{\mathrm{in}}} \,. \tag{28}$$

Here, I_{sc} is the short-circuit current and V_{oc} the open-circuit voltage of the entire BIPV device, i.e. the LSC combined with the solar cell; FF is the fill-factor of the attached solar cell, and P_{in} the total amount of solar power incident on the surface of the LSC. Assuming that these variables scale according to the solar cell's external quantum efficiency (EQE) only, the EQE curves of each PV material can be used to translate solar efficiency into LSC efficiency. Hence, the emission spectrum observed at the perimeter of the LSC is multiplied with a solar cell's EQE curve and integrated to determine I_{sc}.

The power efficiency does not yet tell if the LSC yields a higher efficiency than exposing the PV cells directly to sunlight. A parameter that captures this is the concentration factor [18]

$$\Gamma = G \frac{\eta_{\mathrm{power}}}{\eta_{\mathrm{PV}}} \,, \tag{29}$$

where the geometric gain $G = \frac{A_{\mathrm{LSC}}}{A_{\mathrm{PV}}}$, and η_{PV} is the efficiency of the solar cell when exposed to the AM1.5 spectrum.

To match the output spectrum of an LSC with a solar cell, data on the current record GaAs [33] ($\eta_{\mathrm{PV}} = 27.6\,\%$), CIGS [34] ($\eta_{\mathrm{PV}} = 21.0\,\%$), CdTe [35] ($\eta_{\mathrm{PV}} = 21.0\,\%$), CZSSe [36] ($\eta_{\mathrm{PV}} = 7.6\,\%$), CZTS [36] ($\eta_{\mathrm{PV}} = 9.8\,\%$), Perovskite [36] ($\eta_{\mathrm{PV}} = 22.1\,\%$), Dye [37] ($\eta_{\mathrm{PV}} = 11.9\,\%$), Organic [36] ($\eta_{\mathrm{PV}} = 11.2\,\%$), and Si [38] ($\eta_{\mathrm{PV}} = 25.6\,\%$) cells were used to select the cell which would give the best performance.

First, two generations of MGLT are used to get an indication of what $\alpha_{\max}$ an LSC would be most efficient with when combined with each of the solar cells. From this range the $\alpha_{\max}$ that yields the highest estimated η_{power} adhering to the design-constraints is selected. Finally accurate values for η_{power} and Γ are calculated with MC. The results for the five best performing $100 \times 100 \times 0.5\,\mathrm{cm}^3$ LSCs are shown in Table 3. A theoretical maximum, if there was no concentration quenching, for all LSCs from Table 2 can be found in Data File 2. In the theoretical case, the second maximum of Red305 yields $\eta_{\mathrm{power}}^{\mathrm{GaAs}} = 8.6\,\%$ as maximal power efficiency.

From Table 3 we see that most presented LSCs would already function as efficient PV solar concentrators, evident from $\Gamma \gg 1$. These could be of use in e.g. noise barriers [39], where no clear visible light throughput at the rear of the LSC is required. Also as BIPV windows, in places where no solar cells would otherwise be placed, the LSCs can still perform their function as a BIPV concentrator. Even when a serious constraint of $\eta_{\mathrm{LHE}}^{\mathrm{vis}} = 25\,\%$ is placed on the LSCs, $\Gamma > 1$.

One remark that can be made is that the older LSC materials, Perylene perinone (PP) and Red 305, are still among the most efficient. With the constraint of $\eta_{\mathrm{LHE}}^{\mathrm{vis}} = 25\,\%$ the efficiency of PP does however drop significantly. This is due to the overlap between the visible solar spectrum

Optics EXPRESS

Table 3. Power conversion efficiencies and concentration factors for $100 \times 100 \times 0.5\,\mathrm{cm}^3$ LSC materials with PV cells covering the entire perimeter with $\alpha_{max} = 60\,\mathrm{cm}^{-1}$ (except for Red305, where $\alpha_{max} = 5.5\,\mathrm{cm}^{-1}$ and LumoO with $\alpha_{max} = 7.9\,\mathrm{cm}^{-1}$) and where only 25 % of the visible spectrum is absorbed ($\eta^{vis}_{LHE} = 25\,\%$). Here λ^{out}_{max} is the LSC's output spectrum observed at the perimeter and η^{GaAs}_{power} the highest power efficiency using a GaAs solar cell. η^{alt}_{power} is the best alternative (non-GaAs) cell's power efficiency, with concentration factor Γ^{alt}. Perovskite has been abbreviated to Per.

Material	λ^{out}_{max} (nm)	PV solar concentrator $\alpha_{max} \leq 60\,\mathrm{cm}^{-1}$			BIPV window $\eta^{vis}_{LHE} = 25\,\%$				Best alt. cell
		η^{GaAs}_{power} (%)	η^{alt}_{power} (%)	Γ^{alt}	α_{max} (cm^{-1})	η^{GaAs}_{power} (%)	η^{alt}_{power} (%)	Γ^{alt}	
CdSeCdS	640	4.1	3.3	8.4	12.9	3.0	2.4	6.1	Per.
LumoO	579	*1.4*	*1.1*	*2.8*	7.9	1.4	1.1	2.8	Per.
PP	(743) 720	5.9	4.3	10.2	1.4	1.8	1.3	3.0	CdTe
Red305	642	*3.6*	*2.7*	*7.0*	2.0	2.3	1.8	4.6	Per.
TIIiso	840	3.3	2.9	5.6	2.2	1.2	1.0	2.0	Si

and the absorption of PP being larger than in the other presented LSCs. $\eta^{vis}_{LHE} = 25\,\%$ is therefore a more severe constraint on PP than on any of the other presented materials.

One can also notice the significant redshift observed in the output spectrum of PP when increasing the concentration by more than 40× (noted between parentheses in Table 3). This redshifting can be explained by the large overlap between the absorption and emission spectra of PP.

Optimizing dye concentration with respect to the highest possible η is not always the best approach. For all materials there is a non-constant discrepancy between η and η_{power}. When regarding practical applications it's better to optimize α_{max} with respect to the PV cells available, for maximal power efficiency or concentration factor. We can see that optical efficiency of each material only gives an indication of how well an LSC will perform when connected to a PV element compared to others, i.e. materials with a higher η will also perform better when connected to a solar cell. An example of this is TIIiso. TIIiso has $\eta = 6.7\,\%$ for $\alpha_{max} = 60\,\mathrm{cm}^{-1}$, while its $\eta^{GaAs}_{power} = 3.3\,\%$. This can be explained by the mismatch of the LSC's output spectrum and any PV cell's quantum efficiency curve. Most LSCs will have their peak perimeter-output still within the higher ranges of a PV cell's EQE curve, but due to redshifting from self-absorption, much of the spectrum will fall in the lower EQE region. Another consequence of this redshifted spectrum observed at the perimeter of an LSC, is that the optimal solar cell choice varies widely. This variation puts an emphasis on the need to either design a solar cell for a specific LSC, or, if the LSC were to be designed for use with a specific solar cell, to optimize the redshift of LSC output spectra by altering the LSC's geometry or maximal absorption coefficient.

Variations in materials producing similar η_{power}, but carrying a different concentration factor can be explained by the solar conversion efficiency of the cell. An example of this variation is seen with LumoO and TIIiso. Even with almost the same conversion efficiency for $\eta^{vis}_{LHE} = 25\,\%$, the higher η_{PV} of the Si cell results in a lower concentration factor for LumoO. A similar table could be constructed showing which solar cell would offer the maximum concentration factor. Solar cells with much lower η_{PV} would dominate such a table, as the difference between η_{PV} and η_{power} becomes lower for these cells. Optimization for maximum concentration factor or a compromise situation, yielding quickest return of investment, could be done in a similar fashion.

Optics EXPRESS

7. Conclusions

We have shown that, using a multiple-generation light transport model based on Beer-Lambert's law, light transport without scattering through an LSC of arbitrary geometry can be precisely and fully characterized, with only a relative difference of 4.4 ± 7.7 % between MGLT and MC for 1 m^2 LSCs. Using the MGLT approach, calculating only the first generation of light transport is sufficient to optimize the luminophore concentration of an LSC. The total efficiency of this optimized LSC can then be calculated using MC. Most insight in most materials can however be gained if both models are used in conjunction with each other. The MGLT model can show in great detail what areas of the LSC will contribute to edge transport, whereas MC can more quickly provide an accurate assessment of what efficiencies one could expect. It has been shown that the optimal luminophore concentration is dependent on the size of an LSC. Therefore, an optimized lab-scale LSC's concentration is not transferable to LSCs of different sizes. The power conversion efficiency of 1 m^2 LSCs does not exceed a theoretical 9 % and a practical 6 % for the luminescent materials addressed in this work. These materials can still function very well as BIPV elements, owing to the high concentration factors. As BIPV element, the LSC functions both as a PV solar concentrator and as a semi-transparent power-generating window, which would be complementary to non-transparent solar cells on the building envelope. Finally, we have shown and quantified that for an LSC with a large overlap between its absorption- and emission spectrum, but a high quantum efficiency, self-absorption can be beneficial to its optical efficiency. Photons trapped inside such LSCs will remain trapped until they are redshifted outside of the LSC's absorption spectrum when the LSC has a sufficiently high absorption maximum. The results obtained in this paper can help in designing efficient, aesthetically pleasing LSCs for use in the built environment.

A. Positive self-absorption in MGLT

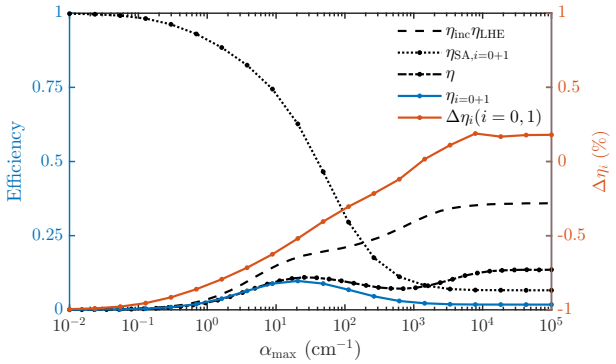

Fig. 7. Optimization track of a 10 × 10 × 0.5 cm^3 Red305 LSC with $\eta_{QY} = 1$. A second maximum is seen in the optical efficiency. Here the second MGLT generation contributes more to the edge-transmission than the first generation.

Optimizing while taking positive self-absorption into account doesn't require calculating the total efficiency of the material. The local maxima occurring due to positive self-absorption can also be observed using the MGLT model with 2 generations. Figure 7 shows that, when $\eta_{QY} = 1$ in Red305, the difference in collected fraction $\Delta\eta_i$ between two generations decreases as the absorption maximum increases. This indicates that the increasing amount of light absorbed between the first to the second generation does not quench or escape, but rather keeps contributing to collection on the perimeter. For sufficiently high α the second generation starts contributing more to total transport than the first, at the same point that the material's optical efficiency η starts

Optics EXPRESS

rising again, giving an indication of a potential efficiency increase due to positive self-absorption.

Funding

Netherlands Organization for Scientific Research (NWO/OCW) (NF16NFS01).